Real-time and Non-contact Estimation of State of Charge for Lithium-ion Battery using Laser Ultrasonics

Santhakumar Sampath, Xuesong Yin, Zi Wen Tham, Yi Fan Chen, and Lei Zhang*

Institute of Materials Research and Engineering (IMRE), Agency for Science, Technology and Research (A*STAR), 2 Fusionopolis Way, Innovis #08-03, Singapore 138634, Republic of Singapore

***** Corresponding author

zhangl@imre.a-star.edu.sg

Abstract

Lithium-ion batteries (LIBs) are widely used in portable electronics, electric vehicles, and stationary storage systems due to their high power and high energy. Monitoring the status of LIBs, particularly the state of charge (SOC), is crucial to ensuring battery performance and safety. Non-destructive ultrasonic approaches are recently emerging as a promising method for estimating the battery state and improving safety. However, current battery state estimation methods require contact and the use of a couplant, limiting their practicality and real-time applications. This study presents a non-contact laser ultrasonic system for monitoring the battery state during charge/discharge cycles. The experimental setup utilizes a line laser source to generate ultrasonic waves and an interferometer to detect the wave signal in a pitch-catch mode. Various ultrasonic features, including time-of-flight (TOF) and signal amplitude (SA), are analyzed in the time and frequency domains, respectively, at different degradation rates. The results show significant changes in the ultrasonic features in response to battery SOC and cycling degradation. The proposed non-contact ultrasonic method has the capability to determine the internal status of LIBs, enabling real-time monitoring of battery safety.

Keywords: Battery safety; State of charge; Laser ultrasonic; Ultrasonic wave; Non-destructive testing; Lithium-ion batteries

1. Introduction

Lithium-ion batteries (LIBs) are extensively applied in various applications, including electronic devices, electric vehicles, and energy storage systems [1-3]. Despite their high performances, ensuring safe operation of LIBs is paramount [4]. For instance, an incident on the Boeing 787 Dreamliner was attributed to a battery failure [5]. A battery management system (BMS) obtains the battery voltage and current to monitor the internal status of the battery, particularly the state of charge (SOC). SOC is significant for evaluating battery degradation and safety [6]. Estimating SOC is a complex task owing to the intricate algorithms in a conventional BMS and nonlinear behavior of batteries. Therefore, it is vital for the BMS to estimate the SOC in real-time and calibrate the capacity regularly [7, 8].

The battery state estimation methods used in a BMS mainly include the Coulomb counting [9], open-circuit voltage (OCV) [10], and model-based [11] methods. However, these methods have limitations such as longer estimation times and reliance on complex algorithms such as the Kalman filter [12, 13]. Conversely, non-destructive testing (NDT) technology has been rapidly developed to assess battery performance and safety. One commonly used NDT method is electrochemical impedance spectroscopy (EIS), which monitors changes in battery impedance as a function of the SOC [14-16]. EIS involves measuring the response of battery impedance to a sinusoidal excitation signal [17]. However, acquiring impedance spectrum data require measurements at a wide range of frequencies, which adds complexity to the computations. Additionally, EIS measurements require a longer testing time and stable test environment, making them inconvenient for real-time applications [18]. On the other hand, fiber optic sensors (FOS), resistant to electromagnetic interference, have been embedded within pouch cells to monitor both internal strain and temperature [19, 20]. Peng et al. [21] applied a designed FOS to a pouch cell surface and explored

the correlation between the strain and SOC. Kalman Filtering algorithm was employed to estimate SOC based on the strain signals obtained from the FOS under different temperature conditions [22]. However, the major drawback of FOS is its reliance on contact SOC measurement. Additionally, FOS can be susceptible to environmental factors such as temperature and humidity, which can affect the accuracy of the strain measurements.

Recent studies have found that de-lithiation and lithiation processes cause a continuous change in both the density and Young's modulus of the electrodes during charge/discharge cycles [23, 24]. Accurately capturing these internal structural alterations contributes to the evaluation of SOC, which is beneficial to a smarter BMS in preventing thermal runaway and improving safety [25]. Ultrasonic-based NDT techniques are being increasingly employed to monitor changes in the physical properties of LIBs during operation [26-28]. Hsieh et al. [29] showed that this technique is viable using time-of-flight (TOF) measurements to investigate the physical dynamics of batteries at different SOC levels. They observed that the changes in the attenuation of the ultrasonic signal indicated variations in the density and bulk modulus of the electrodes within the battery cell. Davies et al. [30, 31] observed the complex reflection of ultrasonic waves in LIBs and identified the fast- and slow-ultrasonic waves for SOC detection. Ladpli et al. [32] used guided waves generated by piezoelectric transducers to facilitate their integration into a BMS. In order to monitor the charging and discharging processes in real-time, a piezoelectric transducer pair was mounted on both sides of the battery surface using an adhesive [33]. Different frequencies (0.9 MHz, 1.8 MHz, and 2.7 MHz) of time-harmonic waves were utilized to capture the dynamic response of batteries at different SOC levels [34]. Anodic oxidation during battery discharge was measured by quantifying the change in the TOF of the ultrasonic signal [35], allowing SOC characterization by analyzing significant changes in the material properties of the battery. An acoustic model was

developed to simulate the change in the battery modulus and density during both de-lithiation and lithiation processes [32]. To understand the variations in the internal structure induced by charge/discharge cycles, a spatially resolved acoustic approach was applied to the batteries [36]. Furthermore, the fundamental shear-horizontal mode of ultrasonic waves was used to monitor the status of the electrodes in a battery [37].

The previous studies have used the contact-based ultrasonic method to generate and detect ultrasonic waves and examine the changes in the internal structures of LIBs. However, this method requires a coupling agent, which may introduce unwanted nonlinearity into the measurements. Moreover, the relatively large size of the transducer poses challenges in accurately detecting the internal status of cylindrical batteries. Most studies have primarily focused on battery cycling under constant current battery cycling, with limited discussion on variations in degradation rates, thereby hindering the practicality of ultrasonic SOC estimation [38, 39]. Maoshu et al. [40] used ultrasonic TOF for SOC estimation under dynamic current conditions; however, this approach required physical contact with the battery.

In this study, a non-contact method for estimating the SOC in LIBs is presented at different battery degradation cycling using laser ultrasonics. The laser ultrasonic system comprises an excitation laser for generating ultrasonic waves and a detection laser for sensing waves in the pitch-catch mode. Ultrasonic features, including TOF in the time-domain and signal amplitude (SA) in the frequency-domain are utilized to assess the internal structures of the battery. The key contributions of this study are: (i) it utilizes a fully non-contact laser ultrasonic technique for battery inspection, (ii) the proposed method can monitor the internal status of the battery in real-time, (iii) it can generate various ultrasonic frequencies to penetrate the battery at different depths, without having access to both sides of the cell, and (iv) the establishment of a correlation between

ultrasonic features and various degradation rates. The paper is structured as follows: Section 2 provides information on the batteries, non-contact laser ultrasonic experimental setup, parameters of data acquisition, and measurement procedure. This section also presents the relationship between ultrasonic features and battery state, as well as the theoretical model of laser-based ultrasonic wave and detection. Section 3 presents the results and discussion from the experiments, along with an evaluation of different battery degradation rates for monitoring battery safety. Finally, Section 4 presents the conclusions.

2. Experimental details

2.1 Batteries and electrochemical cycling

A single pouch-type lithium iron phosphate (LFP, Zon cell) with dimensions of 90 mm × 20 mm × 5 mm is utilized in this study. The nominal capacity and voltage of the battery were 900 mAh and 3.2 V, respectively. The cell was tested within an operating voltage range of 2.5 V to 3.6 V and 2.0 V to 4.0 V at different currents. The experimental setup comprised of: (i) a pouch cell; (ii) battery test equipment (NEWARE BTS-4000) for charging and discharging processes; (iii) temperature acquisition equipment (Graphtec GL840) employed to collect temperature data from the battery surface; and (iv) a non-contact laser ultrasonic system implemented to monitor the battery states in real-time. A constant-current-constant-voltage (CCCV) protocol was employed to perform the charging and discharging operations. For the charging process, the cell was initially charged at a current of 0.6 A until it reached 4.0 V. Then, it was charged at a constant voltage of 4.0 V until the current dropped to 0.06 A. A rest period of 5 min was included between each charging and discharging sequence to enable the pouch cell to achieve equilibrium. For discharge, a current of 0.6 A was maintained until the voltage dropped to 2 V. During the charge/discharge cycling process, the NEWARE software collects data on voltage (V), current (A), and capacity

(Ah) every 30 sec. A temperature data acquisition system was used to measure temperature on the battery surface and ambient temperature. The system utilized K-type thermocouples with a 0.1 °C resolution. Five temperature measurement points were positioned on the battery surface and the temperature data were collected every 10 sec during the battery charge/discharge. The thermocouples transmitted readings to the acquisition system, which was then connected to a computer for data analysis. All the battery cycling and laboratory tests were conducted at room temperature (21.8 °C). The SOC was calculated by subtracting the reference charge (q_{min}) from the final discharge charge (q), and then dividing it by the charge range ($q_{max} - q_{min}$) of the cycle and is expressed as follows:

$$SOC = \frac{q - q_{min}}{q_{max} - q_{min}} \quad (1)$$

2.2 Real-time laser ultrasonic system for charge/discharge test

The proposed laser ultrasonic system for monitoring the battery state mainly includes three parts: a battery tester, a pulsed laser source, and a laser interferometry system, as shown in Fig. 1. An Nd:YAG pulsed laser (NL301G, Ekspla, Lithuania) with a wavelength of 1064 nm, repetition rate of 20 Hz, and maximum pulse energy of 55 mJ was used to generate ultrasonic waves in the cell. The laser beam passed through a cylindrical lens that generated a line source with a width of 0.2 mm. This line source was created in order to obtain the maximal directivity of the ultrasonic wave and facilitate the generation of ultrasonic waves with a high signal-to-noise ratio (SNR) [41]. The generation and detection lasers are arranged on the same side of the cell though pitch catch mode with propagation distance of 15 mm. Ultrasonic waves were excited by the thermoelastic effect and propagated through the cell, where the signal was collected using an interferometer (TEMPO, Bossa Nova Technology) with a wavelength of 532 nm. Through the laser interferometer, the ultrasonic signals were converted from mechanical vibrations to electrical signals, which were

stored by a digital oscilloscope. The laser interferometer also offers a wide frequency bandwidth, ranging from 100 kHz to 200 MHz. To mitigate the effect of noise during the experiment, the pre-processing using Hilbert transform is performed for real-time acquired data and extract the time-domain envelopes in the corresponding SOC and 512 ultrasonic signals were averaged. The ultrasonic data were collected every 5 min during the battery charge/discharge. The battery cell was charged and discharged at different current rates (2.5 V to 3.6 V and 2.0 V to 4.0 V), with experiments conducted at ambient temperature (21.8 °C).

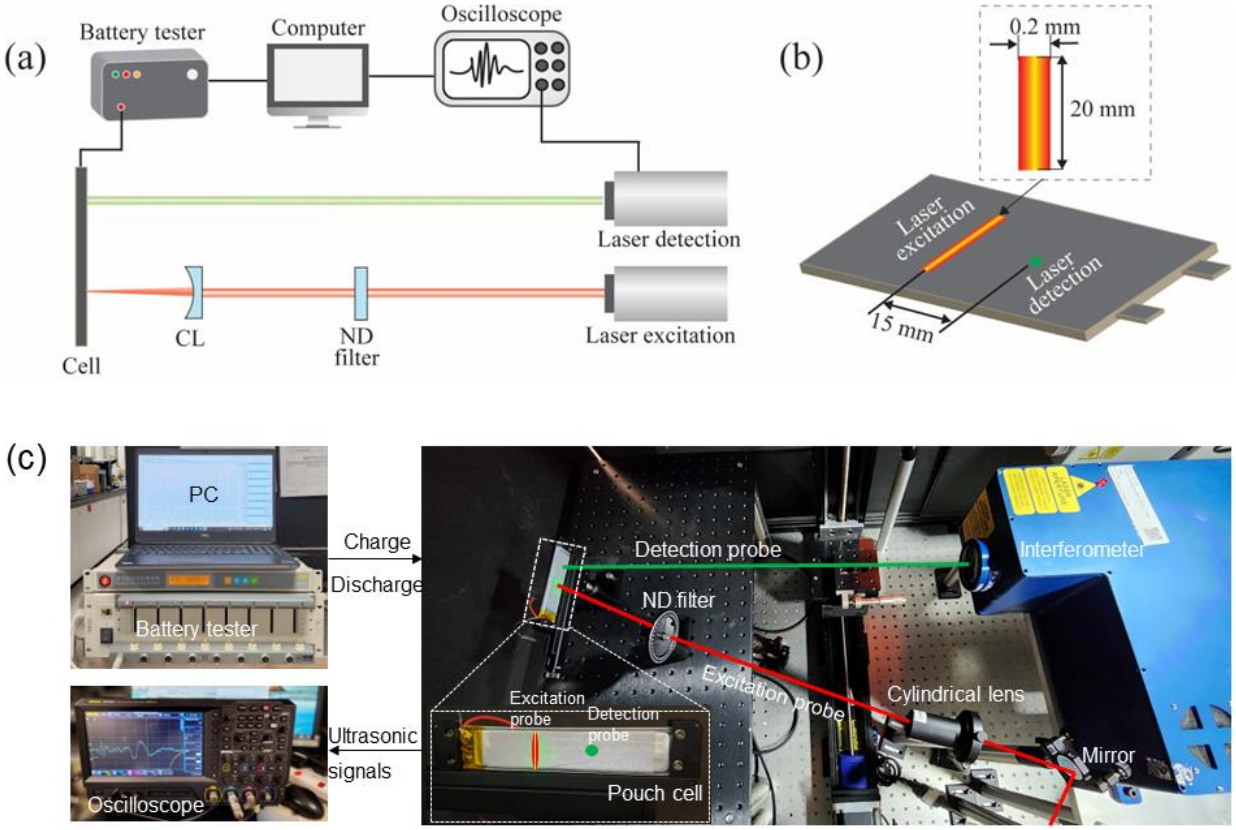

Fig. 1. A non-contact laser ultrasonic system for real-time estimation of the SOC in the pouch cell. (a) schematic diagram of laser system, (b) the position of laser excitation and detection and (c) photograph of experimental setup. CL: Cylindrical lens and ND filter: Neutral density filter.

2.3 Laser line source-based SAW generation

A Nd: YAG laser was used for ultrasonic wave generation, and an interferometry was used to sense out-of-plane wave components. When a laser pulse illuminates the cell surface, the absorbed radiation energy causes localized heating and thermal expansion, generating transient elastic waves. An interferometry measures the frequency or phase difference between an internal reference beam and a test beam reflected from a cell. It correlates the frequency or phase shift to the out-of-plane velocity of the generated ultrasonic waves. In general, laser ultrasound utilizes a point laser source to generate ultrasonic waves in materials via thermal expansion [42-44]. The energy density emitted by a single point source is generally insufficient to directly generate ultrasonic waves due to their propagation in all directions. The amplitude of the single point source is consistently lower than the laser line source for two reasons: (1) the input energy is lower because the illumination area is smaller; and (2) an omnidirectional circular-crested wave is generated whose amplitude decreases as the wavefront becomes larger. However, recent research has shown that using a line laser source can produce powerful ultrasonic waves, thereby overcoming this limitation [45-47]. The line source has two main advantages compared to the point source: (i) high SNR of ultrasonic waves by maintaining more energy in the material; (ii) the energy of the ultrasonic waves generated by the line source is concentrated primarily in the direction perpendicular to the line source, which facilitates energy loss of wave propagation [41]. Therefore, in this study, the single line source was selected which can a reasonably planar wavefront with sufficient amplitudes higher than the single point source. The wavelength of the generated ultrasonic waves is determined by the size of the laser line, provided that the pulse duration of the laser beam is sufficiently short, i.e., where is the wavelength of the elastic waves

generated by a laser beam. Considering the heat equation and ultrasonic wave equation, the thermal conduction can be expressed as [48]

$$\rho C \frac{\partial T}{\partial t} = \nabla \cdot (K \nabla T) + Q \tag{2}$$

where ρ is the material density, C represents the specific heat capacity of the material, T is the temperature increase in the material at time, t, K denotes thermal conduction coefficient and Q is the power density of the heat source generated by the laser line source. The laser beam is assumed to be completely absorbed at the surface in a small volume due to skin effect of the battery materials. Thus, a heat source, Q, ignoring the optical penetration of the incident laser beam is given by:

$$Q = I_0(1 - R) f(x) g(t) \tag{3}$$

where I_0 denotes the peak power density of the incident laser and R is the reflection coefficient of the battery surface. $f(x)$ and $g(t)$ are the spatial and temporal distributions of the incident laser source, respectively and can be expressed as

$$f(x) = \exp\left(-\frac{(x - x_l)^2}{w_0^2}\right) \tag{4}$$

$$g(t) = \exp\left(-\frac{(t - t_0/2)^2}{a_0^2}\right) \tag{5}$$

where x_l and w_0 represent the position and width of the laser source, a_0 denotes the laser pulse rise time, and t_0 is the pulse duration. When a laser pulse illuminates the surface of the battery, the transient displacement field can be described as

$$\mu \nabla^2 \boldsymbol{u} + (\lambda + \mu) \nabla (\nabla \cdot \boldsymbol{u}) - \alpha (3\lambda + 2\mu) \nabla T = \rho \frac{\partial^2 \boldsymbol{u}}{\partial t^2} \tag{6}$$

where λ and μ are Lamé constants, $\boldsymbol{u}$ represents the transient displacement vector of ultrasonic wave due to the thermoelastic effect, $\alpha(3\lambda + 2\mu)$ is the transient force produced by the

temperature gradient. T denotes the temperature field and α is the thermoelastic expansion coefficient of the battery cell.

2.4 Relationship between ultrasonic features and battery state

Batteries are complex structures with multiple layers whose elastic properties such as modulus and density typically change during charge and discharge cycles. These changes are known to influence ultrasonic features such as the TOF (or velocity) and SA (or attenuation) in the response signal [49]. For isotropic elastic materials, the velocity (c) of ultrasonic wave can be expressed as [50]:

$$c = \frac{0.87 + 1.12\nu}{1 + \nu}\sqrt{\frac{E}{2\rho(1 + \nu)}} \tag{7}$$

where E, and ν denote Young's modulus, and Poisson's ratio of the material, respectively. For a battery, the TOF or velocity is determined by the elastic properties of each layer and interface conditions between adjacent layers. During the charging process, the elastic modulus of the cathode tends to decrease, while the anode elastic modulus increases and both densities decrease [51]. The TOF of the battery electrodes is affected by a combination of these parameters [30]. Therefore, TOF is sensitive to changes in the cell layers during charging and discharging processes [52].

SA is another ultrasonic feature used in this study to evaluate the wave attenuation when propagating through various layers, particularly battery electrodes. This attenuation is attributed to multiple factors such as variations in the elastic properties of the electrodes, interface bonding conditions between layers, and beam spreading. The SA of the response signal can be expressed as [53]:

$$A = A_0 e^{-\alpha d} \quad (8)$$

where A_0 is the original amplitude, and A is the amplitude after the propagation distance, d. α is the attenuation coefficient. Previous studies employed the peak amplitude of the time-domain signal to characterize the SA transmitted through the battery [54, 55]. However, the SA is significantly affected by the transducer coupling conditions. In this study, the SA was analyzed in the frequency-domain signal to eliminate the dispersion and coupling effects. The SA due to beam spreading is corrected such that the SA obtained is related only to the battery material properties and structural changes.

3. Results and discussion

3.1 Laser ultrasonic signature and state of charge

The excitation and sensing positions were placed on the surface of the pouch cell, and ultrasonic signals were collected every 5 min during charging, as described in Section 2.2. Figure 2 shows the time- and frequency-domains of the signals when the cell was charged to 100% SOC in the first cycle. The change in the TOF of the time domain and the SA of the frequency domain at 1.125 MHz allow for discrimination between the charged and discharge states. The TOF is determined by calculating the time taken for the ultrasonic wave to travel from excitation to detection in the time domain, while the maximum peak of the ultrasonic wave describes the SA in the frequency-domain signals.

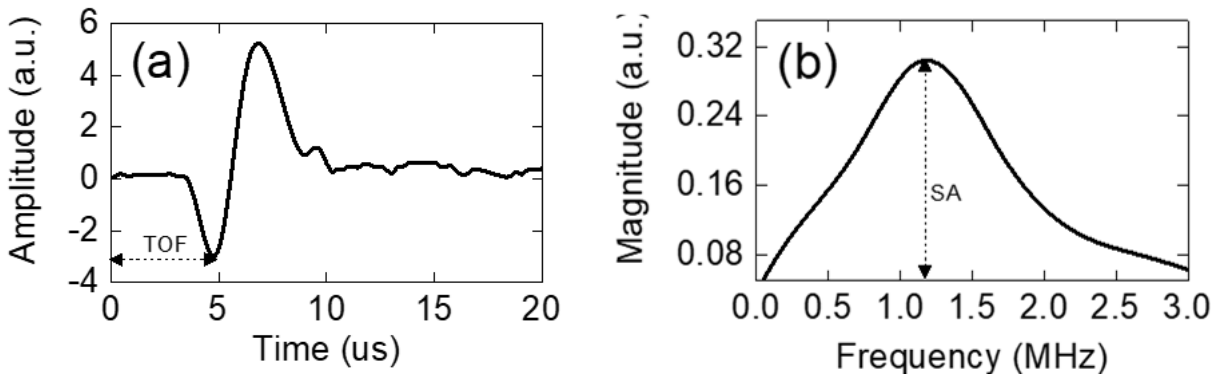

Fig. 2. (a) Time-domain response, (b) the frequency envelope spectra of the response signal determined by a Hilbert transform.

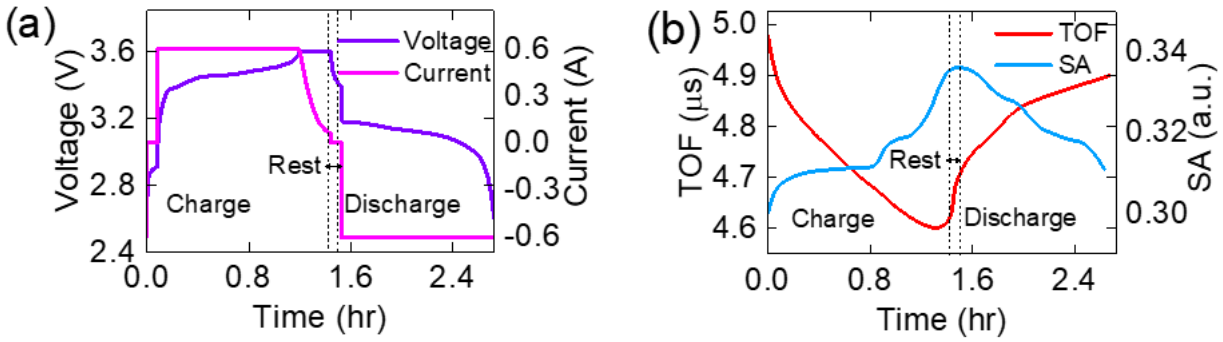

Fig. 3. Battery first charge/discharge profile: (a) voltage and current curves, and (b) change of TOF and SA.

Figure 3 depicts the voltage, current, TOF and SA curves for a charged-discharge process at a current of 600 mA. The voltage range for this process ranges from 2.5 to 3.6 V while maintaining a constant current of 600 mA. The cycle duration for each charge-discharge cycle was of 2.45 h duration. Figure 3(b) displays the relationship between the cycle time and ultrasonic features, demonstrating the shifts in the ultrasonic features during cycling and their synchronization with the electrochemical process. Focusing on the ultrasonic features, we see that the TOF tends to decrease during charging from 0 to 80 min, whereas the SA increases. However, the TOF and SA shifted in opposite directions during the discharge process. These findings are consistent with previously reported results [36, 49, 55].

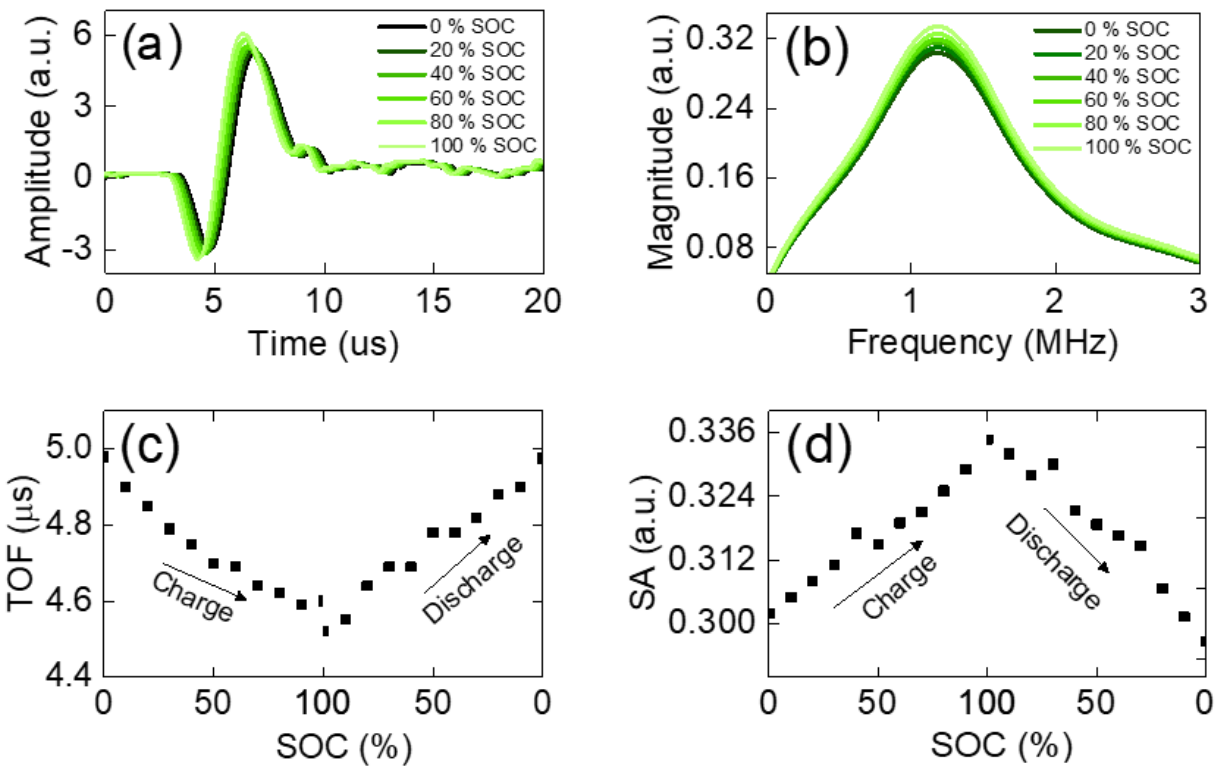

Fig. 4. Ultrasonic responses under different SOC. (a) Time-domain, (b) frequency spectra, (c) TOF and SA.

To further investigate the relationship between the ultrasonic features and SOC, the time-and frequency-domain responses of different SOCs (ranging from 0% to 100% with a 20% increment) were plotted as shown in Figure 4. The time-domain signals clearly demonstrate a decrease in the ultrasonic TOF during charging (Figure 4(a)). Additionally, the frequency-domain signals showed an increase in the SA of ultrasonic wave with a higher SOC. These observations are consistent with previous findings [26, 56, 57] that the de-lithiation/lithiation processes of the cathodes and graphite anodes lead to changes in E, ρ, and ν, ultimately altering the acoustic impedance of the cell and affecting the ultrasonic features. As shown in Figure 4(c), the ultrasonic TOF exhibited a linear decrease as the SOC increased. For instance, when the SOC was 0%, the ultrasonic TOF measures 4.98 μs, but with a SOC of 100%, the TOF decreases to 4.6 μs. Moreover, as the SOC

increased from 0% to 100%, the SA of ultrasonic wave increased by approximately 9.6% (Figure 4(d)) and the TOF decreased by approximately 0.39 μs.

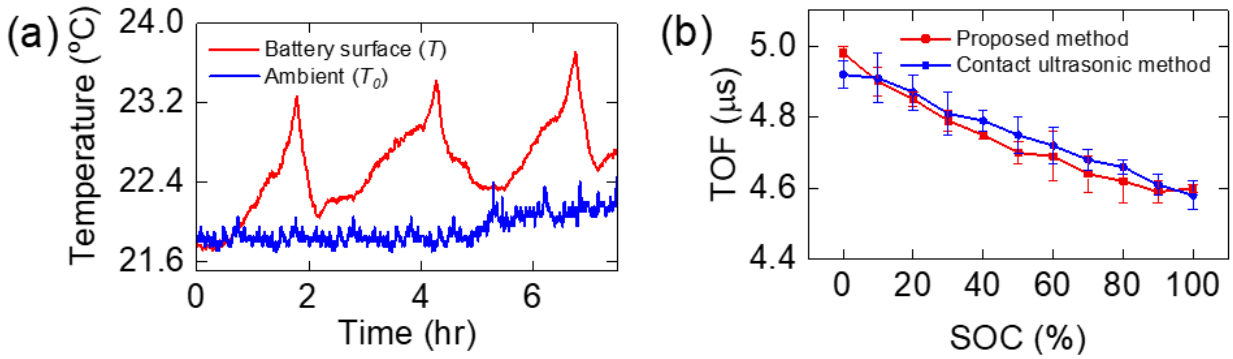

Fig. 5. (a) The battery surface temperature during charge and discharge operations and (b) comparison of the proposed non-contact and conventional contact ultrasonic methods.

Figure 5(a) shows the temperature changes during the charging and discharging cycle, with T representing the battery temperature and T_0 denoting the ambient temperature (21.8 °C). The initial ultrasonic signal before the start of the cycle is used as the reference signal to calculate the TOF (T_0) and ultrasonic signal during charge/discharge cycle is used to determine the TOF (T). Thus, the correlation between TOF and the temperature of the battery surface is expressed as [58]

$$\text{TOF}\ (T) = \text{TOF}\ (T_0) + S\ (T - T_0)$$

where S is the temperature coefficient (μs/°C), which was determined from the average slope of the temperature-TOF curves at various states of charge ranging from 0% to 100%. To study the influence of temperature on the TOF shift, we calculated the TOF at different battery surface temperatures during a 0.6 A cycling test. The averaged slopes were 0.01 μs/°C across the three cycles. It was observed that the variation in TOF (0.22%) caused by temperature effect was very small compared to the TOF shift (7.83%) due to battery degradation. Thus, for the given current rate, the temperature effect on TOF change is negligible in this study. The sensitivity and reliability of the proposed method were validated by comparing its results to those of the contact-based

ultrasonic method under the same battery charge and discharge operations. The conventional ultrasonic tests were performed using a transducer with a cent frequency of 1 MHz. The transducer was driven by a function generator (AFG31000, Tektronix, Inc., USA) to produce the ultrasonic signal. The excitation signal was a seven-period sinusoidal tone burst with a Hanning window, and the voltage was set to 5 V. Before sending the signal to the transmitter, it was amplified 100 times using a power amplifier (US-TXP-3). The ultrasonic transmission signal was recorded using an oscilloscope (TBS 2000B, Tektronix, Inc., USA) with a sampling rate of 100MSA/s. The TOF values obtained from the proposed method were compared with that of the contact-based ultrasonic method at different SOC, as shown in Figure 5(b). Here, the error bar in the experimental results indicates the standard deviation of five measurements taken at different battery SOCs. From Figure 5(b), it is evident that the TOF exhibits a decreasing trend with respect to varying SOC for both methods. Furthermore, the TOF obtained from the proposed method shows reasonable agreement with the conventional ultrasonic results. This agreement validates the efficacy of the proposed non-contact laser ultrasonic technique.

3.2 Battery degradation analysis

Besides performing SOC analysis, the battery was operated at different voltage windows and currents for 300 cycles in order to simulate the degradation process. Throughout the experiments, the laser excitation and detection were consistently maintained at a propagation distance of 15 mm. Battery aging was investigated by evaluating ultrasonic features and SOC at various cycles. The results are shown in Figure 6. The ultrasonic TOF value increased as the number of cycles increased, indicating a delay in the velocity of the ultrasonic waves. This is due to irreversible material degradation resulting from repeated charge/discharge processes. The TOF is consistently higher by 0.31 μs at any SOC on the 150th cycle, signifying an elevation in the aggregate modulus-

to-density ratio of the degraded cells. These changes in the mechanical properties indicate an irreversible transformation in the electrode structure, primarily due to the formation of a solid electrolyte interface (SEI) layer, leading to the irreversible consumption of lithium. The SEI also alters the morphology of the electrode material, leading to changes in the anode modulus and density [59]. It is important to note that battery aging typically involves irreversible swelling, which can be visually observed. The volume expansion in a closed electrochemical cell leads to a reduced total mass density and, consequently, a faster wave velocity. The degradation phenomena observed in the TOF analysis align well with those reported in the literature, indicating lithium loss limiting degradation, accompanied by cathode capacity loss [60, 61].

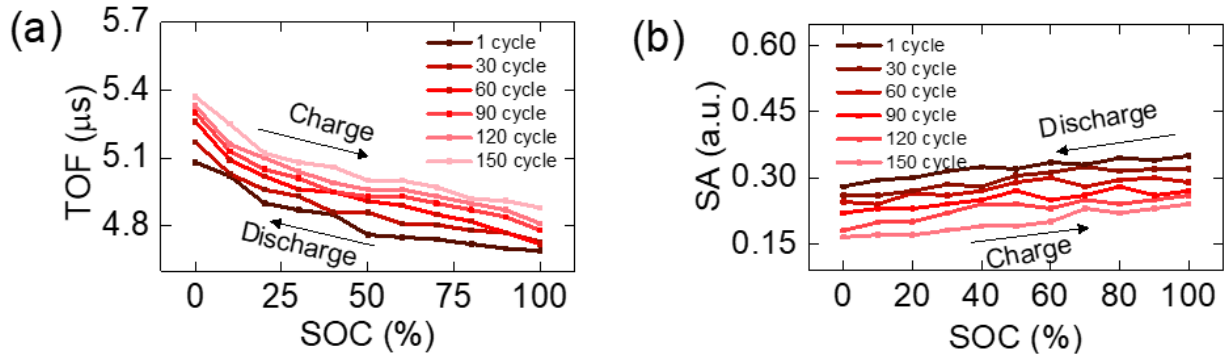

Fig. 6. (a) The envelopes of the received signal with different SOCs and (b) correlation between the TOF history of SAW and SOC.

The SA decreased with each cycle, which suggests that the energy of the initially excited wave was dissipated owing to the aging of the battery from repeated usage (Figure 6(b)). As degradation progressed, the SA continued to decrease, indicating that the mechanical properties changed in each cycle. This decrease in SA was observed at all SOC levels, as previously mentioned by Hsieh et al. in their research [29]. The excessive diffusion of lithium at the interfaces results in compliance changes and lattice strain, leading to an increase in signal attenuation.

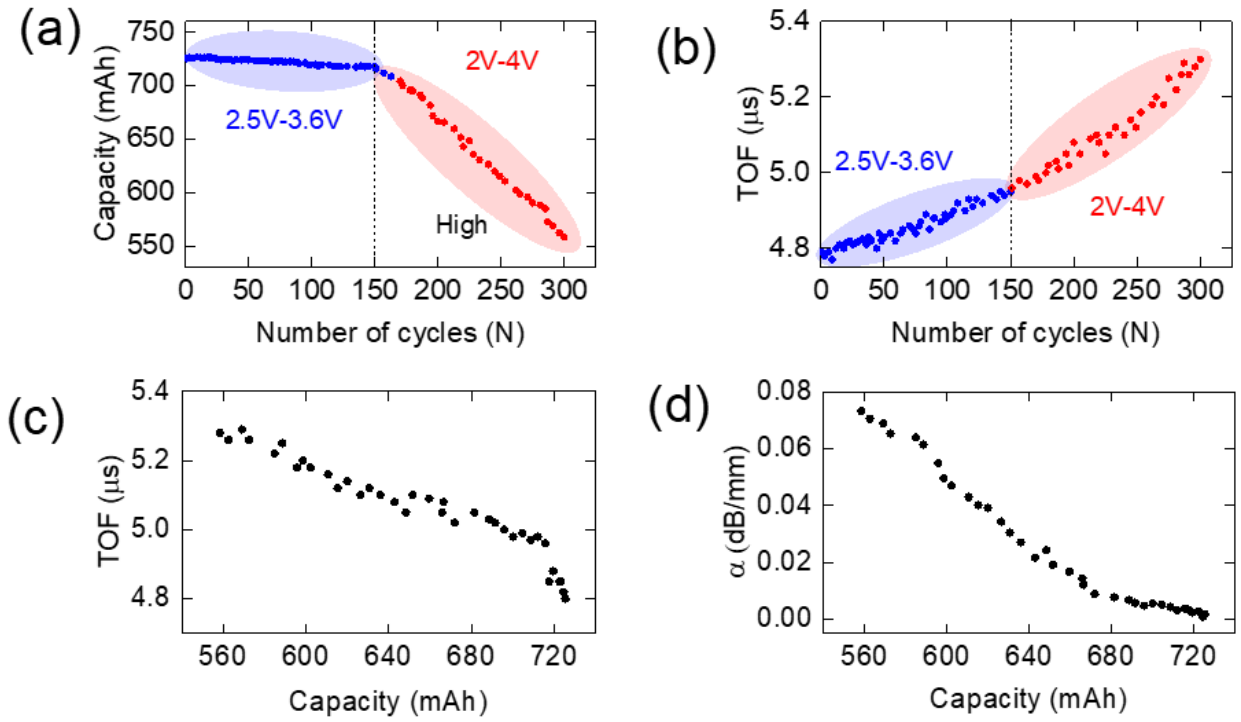

Fig. 7. (a) Capacity decay of the LFP cell cycled at different voltage windows (2.0 V to 4.0 V) and currents, (b) a correlation between TOF and number of charge/discharge cycles, changes of TOF (c) and attenuation coefficient (α) (d) with increasing capacity of cell when SOC is 100%.

The degradation of the battery in relation to the charge/discharge cycles is shown in Figure 7. The capacity of the battery gradually decreased with varying currents, contributing to different levels of degradation. This decline in capacity is attributed to various forms of damage within the electrode material, including lithium precipitation, lattice distortion and reaction layer formation [62]. The TOF value is determined by analyzing ultrasonic wave signals obtained every 5 min during accelerated aging. Figure 7(b) shows the relationship between TOF at SOC of 100% and the number of cycles. Although there is a negligible difference in the TOF between consecutive cycles, it is noteworthy that the overall trend is strongly associated with aging. This suggests a connection between ultrasonic wave characteristics and aging process, indicating that electrochemical degradation is a mechanical phenomenon. Furthermore, a nonlinear relationship exists between the ultrasonic features and battery capacity in Figure 7(c). This change occurred in

two distinct stages (slow degradation rate at 2.5 V to 3.6 V and 0.6 A and fast degradation rate at 2.0 V to 4.0 V and 0.9 A), with a significant drop-off occurring around the 150th cycle. This supports previous findings in the literature, which suggest that the mechanical degradation of the electrodes occurs at an accelerated pace as the battery ages. Throughout the duration of the charge cycling test, changes in TOF and attenuation coefficient (α) were observed when the battery was in a fully charged state at SOC 100% (Figure 7(c)) and α (Figure 7(d)). As degradation occurs, the battery's ability to retain charge decreases. This led to a noticeable increase in the TOF and a decrease in the signal attenuation when the battery was fully charged. The ability to assess battery aging independently from SOC estimation is crucial for developing an on-board degradation evaluation technique. In practical scenarios, such as an idle fully charged electric vehicle, the ultrasonic wave TOF and α can be measured to estimate battery degradation by comparing these parameters with data collected from a set of baseline cells. Another possible application is the use of this ultrasonic technique in conjunction with traditional voltage measurements in existing BMS. The BMS can provide an initial estimate of the SOC, which can then be used as prior knowledge to predict battery degradation. The changes observed in the TOF and SA curves during the charge/discharge cycles demonstrate a strong correlation with the health of the cell.

4. Conclusions

In this paper, real-time monitoring of the internal status of lithium-ion batteries (LIB) using non-contact laser ultrasonics is presented. The ultrasonic wave was created using an excitation laser line source, and its propagation was recorded using an interferometry laser system. The ultrasonic features such as time-of-flight (TOF) and signal amplitude (SA), allow for an effective evaluation of the state of charge (SOC) and aging of the LIB. The TOF parameter is particularly sensitive to the battery SOC, with a linear relationship showing a slope of around 0.38 μs per percent SOC.

The fluctuations in the ultrasonic features are closely correlated with the changes in the physical properties of the electrodes, such as the density and elastic modulus. These fluctuations provide a clear indication of the battery safety. Additionally, the TOF value increases with the number of charge/discharge cycles, suggesting a decrease in the elasticity of the electrode material. The ultrasonic signal energy also attenuated with increasing cycles, and a direct relationship between the ultrasonic features and the number of charge/discharge cycles is established. The variations observed in the TOF and SA curves throughout charge and discharge cycles indicate a significant association between ultrasonic signals and battery states.

CRediT Author Statement

Santhakumar Sampath: Conceptualization, Conducting experiments, Writing - Original Draft. **Yin Xuesong:** Investigation, Resource, Writing – review & editing. **Zi Wen Tham:** Acquisition of data. **Yi Fan Chen**: Acquisition of data. **Lei Zhang**: Methodology, Writing – review & editing.

Acknowledgement

This work was supported by the Singapore National Research Foundation under its Central GAP Fund (Grant Reference NRF2020NRF-CG001-035, Project No. SC25/21-706317) and the Singapore Battery Pack Programme (Project No. M23L6a0020).

References

[1] F. Yang, D. Wang, Y. Zhao, K.-L. Tsui, S.J. Bae, Energy, 145 (2018) 486-495.
[2] J.W. Choi, D. Aurbach, Nature reviews materials, 1 (2016) 1-16.
[3] X. Wan, X. Xu, F. Li, X. Song, C. Peng, J. Liu, Small Structures, (2023) 2300196.
[4] G. Zubi, R. Dufo-López, M. Carvalho, G. Pasaoglu, Renewable and Sustainable Energy Reviews, 89 (2018) 292-308.
[5] K. Liu, Y. Liu, D. Lin, A. Pei, Y. Cui, Science advances, 4 (2018) eaas9820.
[6] Z. Wang, G. Feng, X. Liu, F. Gu, A. Ball, Journal of Energy Storage, 49 (2022) 104124.
[7] B.-b. Sui, L. Sha, P.-f. Wang, Z. Gong, Y.-h. Zhang, Y.-h. Wu, L.-n. Zhao, J.-j. Tang, F.-n. Shi, Journal of Energy Storage, 82 (2024) 110550.
[8] Y. Du, X. Liu, L. Chen, S. Yin, Y. Xie, A. Li, X. Liang, Y. Luo, F. Wu, Y. Mei, Chemical Engineering Journal, 476 (2023) 146605.

[9] H. Huang, J. Meng, Y. Wang, F. Feng, L. Cai, J. Peng, T. Liu, Applied Energy, 322 (2022) 119469.
[10] S. Lee, J. Kim, J. Lee, B.H. Cho, Journal of power sources, 185 (2008) 1367-1373.
[11] N. Wassiliadis, J. Kriegler, K.A. Gamra, M. Lienkamp, Journal of Power Sources, 561 (2023) 232586.
[12] X. Zhang, Y. Tang, F. Zhang, C.-S. Lee, Advanced energy materials, 6 (2016) 1502588.
[13] M. Wang, C. Jiang, S. Zhang, X. Song, Y. Tang, H.-M. Cheng, Nature Chemistry, 10 (2018) 667-672.
[14] A.C. Lazanas, M.I. Prodromidis, ACS Measurement Science Au, (2023).
[15] L. Wang, X. Zhao, Z. Deng, L. Yang, Journal of Energy Storage, 57 (2023) 106275.
[16] W. Choi, H.-C. Shin, J.M. Kim, J.-Y. Choi, W.-S. Yoon, Journal of Electrochemical Science and Technology, 11 (2020) 1-13.
[17] E. Buchicchio, A. De Angelis, F. Santoni, P. Carbone, F. Bianconi, F. Smeraldi, Energy, (2023) 128461.
[18] T. Murariu, C. Morari, Journal of Energy Storage, 21 (2019) 87-93.
[19] L.W. Sommer, P. Kiesel, A. Ganguli, A. Lochbaum, B. Saha, J. Schwartz, C.-J. Bae, M. Alamgir, A. Raghavan, Journal of Power Sources, 296 (2015) 46-52.
[20] L.W. Sommer, A. Raghavan, P. Kiesel, B. Saha, J. Schwartz, A. Lochbaum, A. Ganguli, C.-J. Bae, M. Alamgir, Journal of the Electrochemical Society, 162 (2015) A2664.
[21] J. Peng, X. Zhou, S. Jia, Y. Jin, S. Xu, J. Chen, Journal of Power Sources, 433 (2019) 226692.
[22] A. Ganguli, B. Saha, A. Raghavan, P. Kiesel, K. Arakaki, A. Schuh, J. Schwartz, A. Hegyi, L.W. Sommer, A. Lochbaum, Journal of Power Sources, 341 (2017) 474-482.
[23] D. Zhou, C. Kim, S. Yun, Materials Letters, 224 (2018) 46-49.
[24] Y. Shen, S. Wang, H. Li, K. Wang, K. Jiang, Journal of Energy Storage, 64 (2023) 107164.
[25] S. Wang, Y. Liu, L. He, Y. Sun, Q. Huang, S. Xu, X. Qiu, T. Wei, Chinese Journal of Chemical Engineering, (2024).
[26] J.-Y. Kim, J.-H. Jo, J.-W. Byeon, Microelectronics Reliability, 114 (2020) 113859.
[27] M. Yi, F. Jiang, L. Lu, J. Ren, M. Jin, Y. Yuan, Y. Xiang, X. Geng, X. Zhang, X. Han, International Journal of Energy Research, 46 (2022) 2633-2654.
[28] S.-M. Lee, J.-Y. Kim, J. Lee, J.-W. Byeon, Journal of Materials Research and Technology, 24 (2023) 5235-5249.
[29] A. Hsieh, S. Bhadra, B. Hertzberg, P. Gjeltema, A. Goy, J.W. Fleischer, D.A. Steingart, Energy & environmental science, 8 (2015) 1569-1577.
[30] G. Davies, K.W. Knehr, B. Van Tassell, T. Hodson, S. Biswas, A.G. Hsieh, D.A. Steingart, Journal of The Electrochemical Society, 164 (2017) A2746.
[31] Y. Wu, Y. Wang, W.K. Yung, M. Pecht, Electronics, 8 (2019) 751.
[32] P. Ladpli, F. Kopsaftopoulos, F.-K. Chang, Journal of Power Sources, 384 (2018) 342-354.
[33] L. Gold, T. Bach, W. Virsik, A. Schmitt, J. Müller, T.E. Staab, G. Sextl, Journal of Power Sources, 343 (2017) 536-544.
[34] K. Meng, X. Chen, W. Zhang, W. Chang, J. Xu, Journal of Power Sources, 547 (2022) 232003.
[35] Z. Binpeng, L. Yan, G. Jie, S. Guorong, Z. Yang, L. Yung-chun, H. Cunfu, Ultrasonics, (2023) 107060.
[36] J.B. Robinson, M. Maier, G. Alster, T. Compton, D.J. Brett, P.R. Shearing, Physical Chemistry Chemical Physics, 21 (2019) 6354-6361.
[37] Y. Zhang, H. Dong, T. Wang, G. He, I.P. Parkin, F. Cegla, Journal of Power Sources, 542 (2022) 231730.
[38] X. Cai, X. Li, J. You, F. Yang, Z. Shadike, S. Qin, L. Luo, Y. Guo, X. Yan, S. Shen, Journal of the American Chemical Society, 145 (2023) 25716-25725.
[39] N. Zhao, X. Guo, Science Bulletin, 68 (2023) 1598-1599.
[40] M. Xu, E. Zhang, S. Wang, Y. Shen, B. Zou, H. Li, Y. Wan, K. Wang, K. Jiang, Applied Energy, 355 (2024) 122210.
[41] M. Duquennoy, M. Ouaftouh, M. Qian, F. Jenot, M. Ourak, Ndt & E International, 34 (2001) 355-362.
[42] H. Liu, L. Zhang, H.F. Liu, S. Chen, S. Wang, Z.Z. Wong, K. Yao, Ultrasonics, 89 (2018) 166-172.
[43] Q.Y.S. Wu, N. Zhang, W.H. Liew, V. Lim, X. Ni, L. Zhang, B. Russell, L. Ke, Journal of Composite Materials, 55 (2021) 3241-3251.
[44] N. Podymova, I. Kalashnikov, L. Bolotova, L. Kobeleva, Ultrasonics, 99 (2019) 105959.
[45] S. Kenderian, B.B. Djordjevic, R.E. Green, IEEE transactions on ultrasonics, ferroelectrics, and frequency control, 50 (2003) 1057-1064.
[46] Y. Sohn, S. Krishnaswamy, The Journal of the Acoustical Society of America, 115 (2004) 172-181.
[47] D. Royer, Ultrasonics, 39 (2001) 345-354.
[48] X. Liang, B. Lin, Z. Liu, X. Ma, Applied Acoustics, 199 (2022) 109028.
[49] H. Sun, N. Muralidharan, R. Amin, V. Rathod, P. Ramuhalli, I. Belharouak, Journal of Power Sources, 549 (2022) 232091.

[50] F. Qin, B. Li, L. Chen, Z. Shang, Materials Chemistry and Physics, 242 (2020) 122523.
[51] S. Feiler, P. Daubinger, L. Gold, S. Hartmann, G.A. Giffin, Batteries & Supercaps, 6 (2023) e202200518.
[52] T. Yamanaka, H. Nakagawa, S. Tsubouchi, Y. Domi, T. Doi, T. Abe, Z. Ogumi, Electrochemistry Communications, 77 (2017) 32-35.
[53] D. Williams, R. Copley, P. Bugryniec, R. Dwyer-Joyce, S. Brown, Journal of Power Sources, 590 (2024) 233777.
[54] G. Jie, Z. Liangheng, L. Yan, S. Fan, W. Bin, H. Cunfu, Journal of Energy Storage, 72 (2023) 108384.
[55] G. Zhao, Y. Liu, G. Liu, S. Jiang, W. Hao, Journal of Energy Storage, 39 (2021) 102657.
[56] X. Li, C. Wu, C. Fu, S. Zheng, J. Tian, Energies, 15 (2022) 6027.
[57] Q. Ke, S. Jiang, W. Li, W. Lin, X. Li, H. Huang, Journal of Power Sources, 549 (2022) 232031.
[58] A.S. Borujerdi, C. Jin, J. Zhu, Journal of Power Sources, 597 (2024) 234103.
[59] P.B. Balbuena, Y.X. Wang, Lithium-ion batteries: solid-electrolyte interphase, World Scientific, 2004.
[60] J. Wang, J. Purewal, P. Liu, J. Hicks-Garner, S. Soukazian, E. Sherman, A. Sorenson, L. Vu, H. Tataria, M.W. Verbrugge, Journal of Power Sources, 269 (2014) 937-948.
[61] J. Cannarella, C.B. Arnold, Journal of Power Sources, 269 (2014) 7-14.
[62] J. Kim, K. Yoo, D. Kim, M. Lee, W. Yang, J. Byeon, Microelectronics Reliability, 100 (2019) 113441.